

OffsetCrust: Variable-Radius Offset Approximation with Power Diagrams

Zihan Zhao , Pengfei Wang , Minfeng Xu , Shuangmin Chen , Shiqing Xin* , Changhe Tu ,
and Wenping Wang  *Fellow, IEEE*



Abstract—Offset surfaces, defined as the Minkowski sum of a base surface and a rolling ball, play a crucial role in geometry processing, with applications ranging from coverage motion planning to brush modeling. While considerable progress has been made in computing *constant-radius* offset surfaces, computing *variable-radius* offset surfaces remains a challenging problem. In this paper, we present *OffsetCrust*, a novel framework that efficiently addresses the variable-radius offsetting problem by computing a power diagram. Let \mathcal{R} denote the radius function defined on the base surface \mathcal{S} . The power diagram is constructed from contributing sites, consisting of carefully sampled base points on \mathcal{S} and their corresponding off-surface points, displaced along \mathcal{R} -dependent directions. In the constant-radius case only, these displacement directions align exactly with the surface normals of \mathcal{S} . Moreover, our method mitigates the misalignment issues commonly seen in crust-based approaches through a lightweight fine-tuning procedure. We validate the accuracy and efficiency of OffsetCrust through extensive experiments, and demonstrate its practical utility in applications such as reconstructing original boundary surfaces from medial axis transform (MAT) representations.

Index Terms—digital geometry processing, variable-radius offset, power diagram, medial axis transform

1 INTRODUCTION

Offset surfaces, defined as the Minkowski sum of a base surface and a rolling ball [1], with either constant or varying radius, play a fundamental role in geometry processing. They support a wide range of applications, including motion planning [2] and brush-stroke simulation [3], as illustrated in Figure 1(a,c).

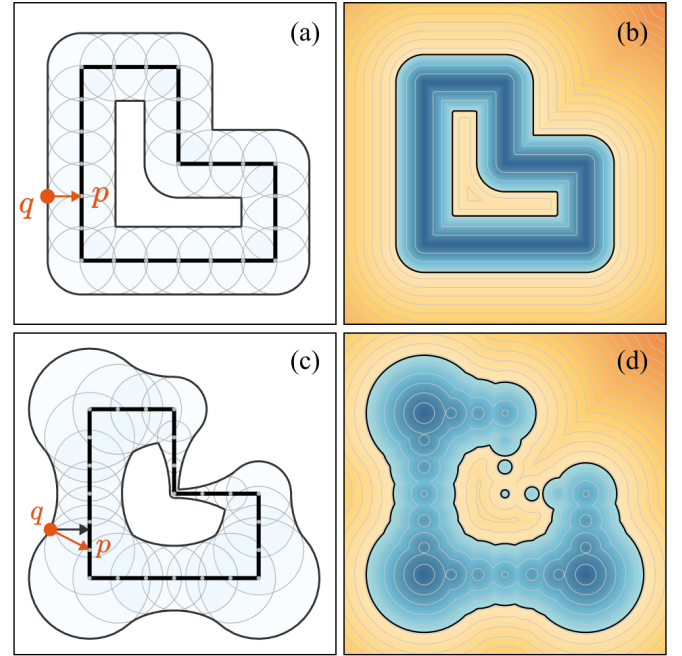


Fig. 1: Offsetting a solid “L”. (a) Constant-radius offset: for a point q , the minimizer p coincides with the closest point on the surface. (b) The offset surface can be defined as the iso-surface of the corresponding distance function. (c) Variable-radius offset: for a point q , the minimizer p may differ from the closest point. (d) Approximating Eq. (1) by simply replacing the continuous boundary with a set of sample points leads to noticeable artifacts. Moreover, this naïve approximation incurs a high computational cost.

- Zihan Zhao, Pengfei Wang, Shiqing Xin, and Changhe Tu are with the School of Computer Science and Technology, Shandong University, Qingdao 266237, China (e-mail: zihanzhao2000@gmail.com; pengfei1998@foxmail.com; xinshiqing@sdu.edu.cn; chtu@sdu.edu.cn).
- Minfeng Xu is with School of Computer Science and Technology, Shandong University of Finance and Economics, Jinan 250014, China (e-mail: mfxu_sdu@163.com).
- Shuangmin Chen is with the School of Information and Technology, Qingdao University of Science and Technology, Shandong 266101, China (e-mail: csmqq@163.com).
- Wenping Wang is with the Department of Computer Science and Engineering, Texas A&M University, College Station, TX 77843 USA (e-mail: wenping@tamu.edu).
- *Shiqing Xin is the corresponding author.
- Manuscript received April 19, 2021; revised August 16, 2021.

Given a base surface \mathcal{S} and a radius function \mathcal{R} defined on \mathcal{S} , the offsetting problem can be formulated as an iso-surface extraction problem. We define a generalized distance function as follows:

$$\phi(x) := \min_{p \in \mathcal{S}} (\|x - p\| - \mathcal{R}(p)), \quad (1)$$

and extract the offset surface $\mathcal{S}_{\mathcal{R}}^{\text{off}}$ as the zero level set, i.e., $\phi(x) = 0$. In particular, when \mathcal{S} is closed and orientable, $\mathcal{S}_{\mathcal{R}}^{\text{off}}$ can be further divided into inward and outward offset layers.

As shown in Figure 1(a,b), a straightforward yet important observation is that, in the constant-radius case, the nearest point on \mathcal{S} serves as the minimizer of the generalized distance. As a result, the offset surface coincides exactly with the iso-surface of the unsigned distance function of \mathcal{S} , evaluated at a fixed offset value. This property underpins most existing approaches [4]–[13] to constant-radius offsetting. Given the significance of this task, several recent methods [14], [15] have been proposed to improve surface quality and runtime performance. However, these methods are not applicable to the more general and challenging case of variable-radius offsetting.

As shown in Figure 1(c), we assign a non-uniform radius function to the boundary and visualize the resulting true variable-radius offset. In this scenario, for a point q , the minimizer p may differ from the closest point on the surface, typically deviating from the surface normal at an angle. A naïve approach to approximate Eq. (1) is to replace the continuous boundary with a set of sampled points. However, this approximation introduces noticeable artifacts (see Figure 1(d)) and incurs a high computational cost.

In previous research, very few works have explicitly tackled this challenge. Some existing methods define variable-radius offsets differently, by specifying the displacement amount along surface normals. These approaches are typically formulated on parametric curves and surfaces [16]–[19]. However, they are not applicable when only a radius function is provided and must also contend with the complex issue of self-intersections [20].

The goal of this paper is to develop an efficient algorithm for the variable-radius offsetting problem that produces geometrically and topologically accurate results. Moreover, the sharp features inherent in the offset surface should be faithfully preserved. To this end, we propose *OffsetCrust*, a crust-based framework designed to achieve these objectives. Our method proceeds as follows: we sample a sufficient number of points from the base surface and displace them along specially designed directions, computed based on the variation of the radius function \mathcal{R} . By assigning different weights to base points and displaced points, the variable-radius offset can be effectively approximated as the subset of power diagram facets that separate these two types of sites (see Section 3).

We further introduce a carefully designed sampling strategy (see Section 4) and a refinement technique (see Section 4.2) to address the misalignment issues inherent in crust-based methods. We validate the effectiveness of our approach through extensive experiments (see Section 5) and demonstrate its utility in several modeling tasks (see Section 6).

2 RELATED WORK

2.1 Constant-Radius Offset

There is a large body of literature addressing the problem of constant-radius offsets. We categorize these approaches into four main groups.

Parametric Offsets. Parametric curves and surfaces are widely used in CAD/CAM as continuous shape representations. In this setting, both the base surface and its offset can be analytically expressed, typically using B-spline curves

or NURBS surfaces. A constant-radius offset displaces each point along the surface normal by a fixed distance d , given by $\hat{\mathbf{r}}(t) = \mathbf{r}(t) + d\mathbf{n}(t)$ [16]–[18]. However, this method requires tedious handling of self-intersections.

Voxelization Representations. Constant-radius offsets can also be computed via the Minkowski sum of the shape with a discrete sphere. Li et al. [23]–[25] proposed GPU-accelerated approximations using voxelization. Beyond the Minkowski sum, Chen et al. [8] employed dixel structures [26] for parallelizable offset computation. While voxel-based methods are easy to implement, they often suffer from high computational cost, limited accuracy, and the loss of sharp features.

Distance Fields. Constant-radius offsets can be represented as level sets of signed distance fields (SDFs). Given a well-computed SDF (typically defined over a grid), the offset surface becomes an iso-surface extraction problem. Numerous works have explored this approach [4]–[7], [9]–[13]. To improve accuracy and preserve sharp features, various enhancements have been proposed. Qu et al. [27] used offset distance fields with irregular, dense grids. Pavic et al. [28] employed a variant of Dual Contouring [6], although their method struggled in concave regions. Zint et al. [15] combined topology-adapted octrees with Dual Contouring and remeshing to produce high-quality meshes, though self-intersections remained unresolved.

Generalized Voronoi Diagrams. Polygonal curves and surfaces are commonly used as discrete shape representations. Generalized Voronoi diagrams, constructed using line segments, circles, and arcs as sites, have been applied to compute constant-radius offsets for 2D polygons [3], [29]–[31]. These diagrams partition the plane into curved cells, with the offset in each cell determined solely by its associated site. However, extending such diagrams to 3D remains a significant challenge.

2.2 Variable-Radius Offset

Compared to constant-radius offsets, relatively few algorithms have been developed for variable-radius offsets, most of which focus on parametric inputs. Kim et al. [19] extended the concept of offsets to parametric surfaces with variable radii, but their approach is not applicable when only a radius function is given. Qun et al. [32] introduced explicit formulas for computing the envelope of balls, enabling exact representation of variable-radius offsets—but at the cost of handling complex self-intersections.

For general triangle meshes, a common strategy approximates the offset surface as the union of primitives: spheres at vertices, cones along edges, and slabs on faces. Due to the high computational cost of this strategy, Woerl et al. [33] proposed a discretized, GPU-accelerated volumetric method, which still suffers from geometric inaccuracy.

2.3 Crust-Based Methods

Crust-based methods typically rely on pairs of seed points to define a surface that separates one set of seeds from another, generally requiring the explicit construction of a Voronoi or power diagram. Careful seed placement is essential to prevent misaligned facets.

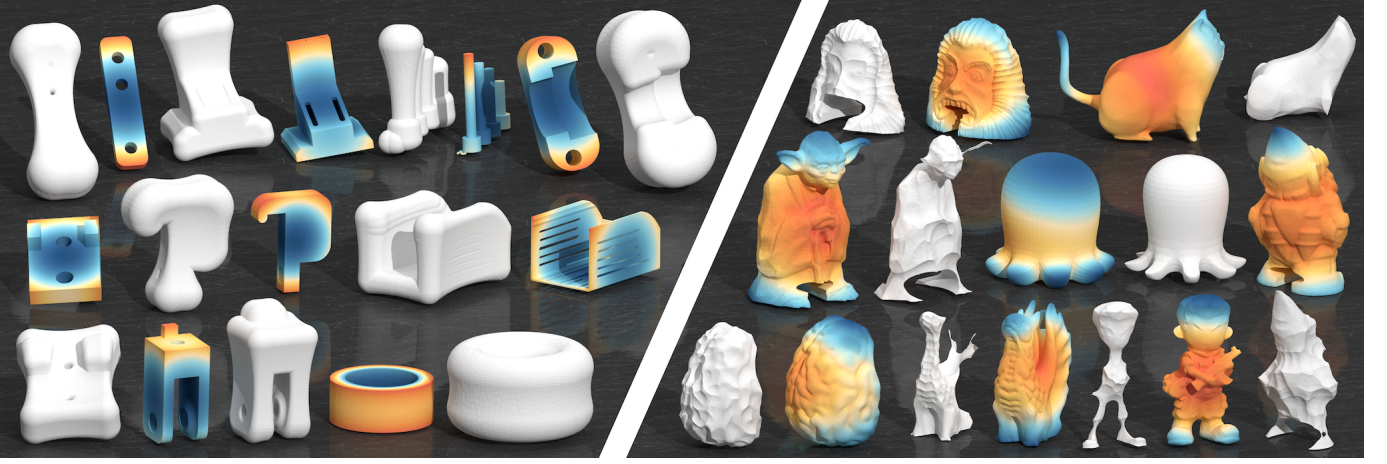


Fig. 2: A gallery of variable-radius offset surfaces computed by our *OffsetCrust*. The offset distances (visualized using different colors) are generated using the quadratic function $\frac{1}{15}\|v\|^2 + 0.01$, with models normalized to the cube $[-1, 1]^3$. Left: CAD models from the ABC dataset [21] and their outward offsets. Right: Freeform models from Thingi10K [22] and their inward offsets.

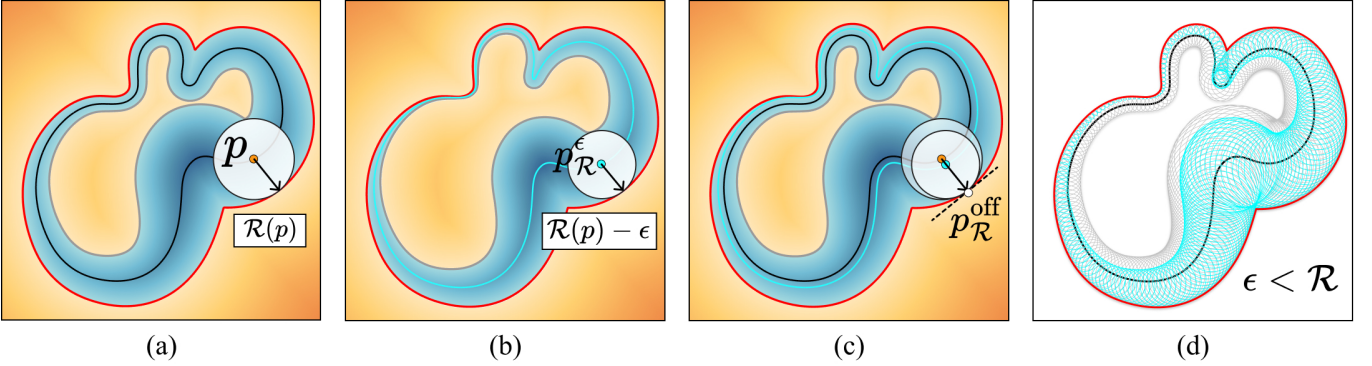


Fig. 3: Insight into why the power diagram helps determine the variable-radius offset. (a) A point p on the base surface; (b) A displaced point p_R^ϵ , located along the \mathcal{R} -dependent direction at a small distance ϵ ; (c) The three points p , p_R^ϵ , and the corresponding point on the offset surface p_R^{off} are colinear; (d) Visualization of the balls centered at the base sample points (gray) and those centered at the displaced points (cyan). The value ϵ can be chosen sufficiently small, or at least not exceeding the specified radius. In the power diagram, the bisector between p and p_R^ϵ typically defines the tangent line at p_R^{off} .

PowerCrust [34] uses the Voronoi diagram of sample points to approximate the medial axis transform (MAT), identifying interior and exterior poles. The power diagram of these poles is then used to reconstruct the surface and approximate constant-radius offsets. VoroCrust [35], [36] improves robustness by employing co-circular or co-spherical sampling strategies to reduce misalignment.

3 INSIGHT

We explain why power diagrams can be used to solve the variable-radius offsetting problem. Suppose we are given a smooth surface \mathcal{S} , typically discretized as a triangular mesh \mathcal{M} , along with a user-specified radius function \mathcal{R} .

3.1 Continuous Setting

Given a smooth, closed, and orientable surface \mathcal{S} , and any positive radius function $\mathcal{R} > 0$, the offset surface $\mathcal{S}_{\mathcal{R}}^{\text{off}}$ consists of inward and outward layers. Each point $p \in \mathcal{S}$

induces a ball centered at p with radius $\mathcal{R}(p)$. As the offset surface is the envelope of these rolling balls, any point q on the surface of the ball centered at p either lies on the final offset surface or is occluded by another ball.

As shown in Figure 3, assume a point $p \in \mathcal{S}$ contributes to $\mathcal{S}_{\mathcal{R}}^{\text{off}}$, yielding a corresponding offset point p_R^{off} . The segment pp_R^{off} lies entirely within the band between the inward and outward layers. The direction of this segment, denoted $\mathbf{n}_{\mathcal{R}}^{\text{off}}(p)$, may differ from the surface normal at p .

Let $\epsilon > 0$ be sufficiently small, and define:

$$p_R^\epsilon := p + \epsilon \cdot \mathbf{n}_{\mathcal{R}}^{\text{off}}(p). \quad (2)$$

Then, the three points p , p_R^ϵ , and p_R^{off} are colinear. We thus obtain:

$$\|p_R^{\text{off}} - p\| - \mathcal{R}(p) = \|p_R^{\text{off}} - p_R^\epsilon\| - (\mathcal{R}(p) - \epsilon) = 0, \quad (3)$$

or equivalently:

$$\|p_R^{\text{off}} - p\|^2 - \mathcal{R}^2(p) = \|p_R^{\text{off}} - p_R^\epsilon\|^2 - (\mathcal{R}(p) - \epsilon)^2 = 0. \quad (4)$$

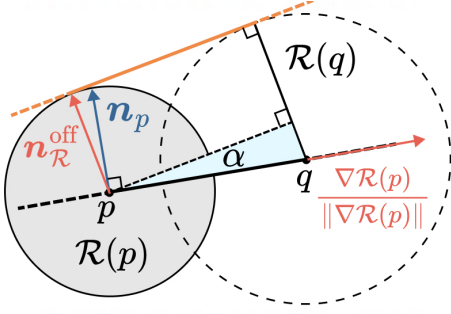


Fig. 4: Proof to Theorem 1.

This motivates the construction of two groups of points and the use of a power diagram to determine the offset surface; see Figure 3. In particular, the bisector between p and p_R^ϵ typically defines the tangent line at p_R^{off} . As for the choice of ϵ , its value can be made sufficiently small, or at most equal to the specified radius.

3.2 Discrete Representation via Power Diagram

Power Diagram. Given a set of weighted points (also called *sites*)

$$\{(p_i, w_i) \mid p_i \in \mathbb{R}^3, w_i \in \mathbb{R}\}_{i=1}^n, \quad (5)$$

the power diagram [37] partitions \mathbb{R}^3 into (possibly unbounded) convex regions. Each region Ω_i , corresponding to a site (p_i, w_i) , contains all points $x \in \mathbb{R}^3$ minimizing the power distance:

$$d_{p_i}^{\text{pow}}(x) = \|x - p_i\|^2 - w_i. \quad (6)$$

In our setting, we construct the power diagram using:

- Points sampled from the base surface, each with weight $\mathcal{R}^2(p)$;
- Displaced points offset in the direction $\mathbf{n}_{\mathcal{R}}^{\text{off}}(p)$, each with weight $(\mathcal{R}(p) - \epsilon)^2$.

The computation of $\mathbf{n}_{\mathcal{R}}^{\text{off}}(p)$ is described next.

Displacement Direction. As previously noted, the displacement direction $\mathbf{n}_{\mathcal{R}}^{\text{off}}(p)$ may not align with the surface normal. Instead, it depends on the radius function \mathcal{R} .

Theorem 1 (Displacement Direction). If $\|\nabla \mathcal{R}(p)\| \leq 1$, the offset direction $\mathbf{n}_{\mathcal{R}}^{\text{off}}(p)$ at point p can be constructed by rotating the unit normal \mathbf{n}_p by an angle $\alpha = \arcsin(\|\nabla \mathcal{R}(p)\|)$ around the axis

$$\frac{\nabla \mathcal{R}(p)}{\|\nabla \mathcal{R}(p)\|} \times \mathbf{n}_p. \quad (7)$$

Proof. As illustrated in Figure 4, let p and q be a pair of nearby points on the surface. Each point defines a sphere centered at itself, with radii $\mathcal{R}(p)$ and $\mathcal{R}(q)$, respectively.

We consider the right triangle highlighted in Figure 4. The hypotenuse has length $\|pq\|$, and one leg has length $|\mathcal{R}(p) - \mathcal{R}(q)|$. This leg lies in the direction of the gradient $\nabla \mathcal{R}(p)$, while the other leg lies in the tangent plane at the offset point p_R^{off} . Given this geometric configuration, the angle α , and hence the displacement direction, can be computed directly.

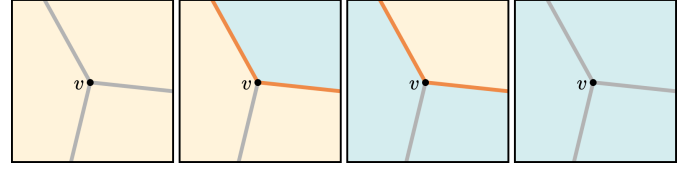


Fig. 5: We illustrate the manifoldness of the output using a 2D power diagram. Since the offset surface is extracted as the separator between base points and displaced points, it is straightforward to verify that non-manifoldness cannot occur by exhaustively examining all four competing configurations.

Manifold Output Without the Need for Explicit Self-Intersection Handling. Without loss of generality, we assume the power diagram does not exhibit degeneracies—specifically, no more than three sites determine a Voronoi vertex in 2D, and no more than four in 3D. Figure 5 shows four representative configurations, where the regions corresponding to base points and displaced points are visualized in different colors. It is straightforward to verify that non-manifoldness cannot occur by examining all possible configurations.

Furthermore, unlike traditional offsetting methods that require explicit handling of self-intersections, our approach avoids this complication entirely. Let p be a sample point on the base surface that does not contribute to the final offset surface—that is, its corresponding offset point p_R^{off} lies strictly inside the envelope. We now explain why such a point cannot contribute to the crust, and thus requires no special treatment.

Since p_R^{off} lies within the interior of the envelope, there must exist another point q whose associated ball contains p_R^{off} . This implies:

$$\|q - p_R^{\text{off}}\| < \mathcal{R}(q), \quad (8)$$

or, equivalently,

$$\|q - p_R^{\text{off}}\| - \mathcal{R}(q) < 0. \quad (9)$$

Therefore, we further have

$$\|p - p_R^{\text{off}}\| - \mathcal{R}(p) = 0 > \|q - p_R^{\text{off}}\| - \mathcal{R}(q), \quad (10)$$

or

$$\|p - p_R^{\text{off}}\|^2 - \mathcal{R}^2(p) = 0 > \|q - p_R^{\text{off}}\|^2 - \mathcal{R}^2(q), \quad (11)$$

or

$$d_p^{\text{pow}}(p_R^{\text{off}}) > d_q^{\text{pow}}(p_R^{\text{off}}), \quad (12)$$

which shows that p_R^{off} must reside in the power cell of q (or of another, more dominant site). To summarize, the point p must be located in the interior of the envelope and thus does not contribute to the crust.

Misaligned Facets. As shown in Figure 6, crust-based approaches are prone to misalignment issues. Suppose p and q are a pair of nearby points. Point p (resp. q) induces a facet with surface normal $\mathbf{n}_{\mathcal{R}}^{\text{off}}(p)$ (resp. $\mathbf{n}_{\mathcal{R}}^{\text{off}}(q)$) at the offset point p_R^{off} (resp. q_R^{off}). However, a gap may exist between the two facets, often filled by the bisector defined by either the pair (p, q_R^ϵ) or the pair (q, p_R^ϵ) .

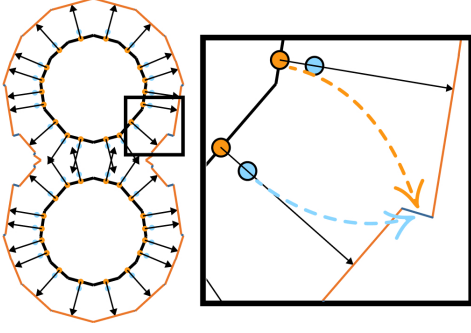


Fig. 6: Crust-based approaches are prone to misalignment issues, where the misaligned segment (shown in blue) is formed by a base point and the displaced point of a different base point.

VoroCrust [35], [36] addresses such misalignments by carefully positioning the sample points. However, it is limited to representing the base surface itself. In our scenario, we instead use a power diagram to represent the offset surface. While it is challenging to design a “perfect” sampling strategy that eliminates all misalignments, we propose a refinement technique (Section 4.2) to effectively suppress them. Further discussion is provided in Appendix B.

Requirements on \mathcal{R} . The user-specified radius function \mathcal{R} must satisfy certain requirements. The key condition is that $\|\nabla\mathcal{R}(p)\| \leq 1$, as required by Theorem 1, where only values satisfying this constraint yield a valid angle $\alpha = \arcsin(\|\nabla\mathcal{R}(p)\|)$. This condition is also consistent with reconstruction from the medial axis transform (MAT). If $\|\nabla\mathcal{R}(p)\| > 1$, then in the neighborhood of p , there exists another point q such that the medial ball of p contains that of q , or vice versa—contradicting the MAT property of maximal, non-nested balls.

When the input is a triangle mesh, the radius function \mathcal{R} is typically defined at the vertices. We assume that \mathcal{R} is a linear scalar field within each triangle. In practice, users may provide values at only a sparse subset of vertices. The remaining values can then be smoothly interpolated by solving the biharmonic equation $\Delta^2\mathcal{R} = 0$ over the mesh surface.

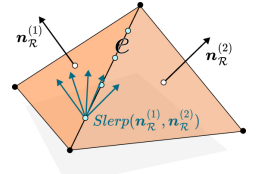
4 IMPLEMENTATION

4.1 Sampling

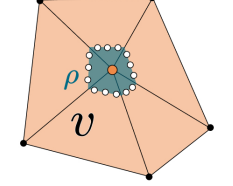
In the previous section, we assumed that surface normals undergo a smooth transition. However, when the input is a triangle mesh, surface normals may exhibit abrupt changes across sharp feature lines. Therefore, it is necessary to carefully address the sampling problem.

In general, base sample points can be categorized into three types: triangle-interior points, edge-type points, and vertex-type points. Triangle-interior points are generated using a blue-noise sampling process. For each triangle-interior point, we generate a unique displaced point based on Theorem 1. In contrast, for edge-type and vertex-type points, we adopt a “one base point, multiple displaced points” (1vN) strategy.

Edge-Type Base Points. For the sake of algorithmic generality, we do not explicitly detect sharp feature lines. Instead, all mesh edges and vertices are treated uniformly. The inset figure illustrates the 1vN strategy for generating base points and their corresponding displaced points. Consider a manifold edge e shared by two triangle faces f_1 and f_2 . For a point on e , the estimated displacement directions $\mathbf{n}_{\mathcal{R}}^{(1)}$ and $\mathbf{n}_{\mathcal{R}}^{(2)}$ may differ depending on whether the estimation is performed within f_1 or f_2 . Once these directions are computed, we generate multiple displacement directions by interpolating between them. This is efficiently implemented using spherical linear interpolation (Slerp).

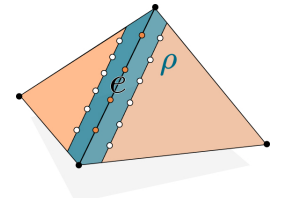


Vertex-Type Base Points. For each vertex v , we place a small sphere centered at v such that it intersects the base surface along a closed trajectory; see the inset figure. By extracting a set of sample points from this trajectory, we can apply Slerp to generate the corresponding displaced points. In practice, this process can be efficiently implemented using an alternative strategy: select a group of sample points around v , and adjust their distances to v to match a prescribed value. Typically, we set the radius of the small sphere to $\rho \cdot l$, where l denotes the average edge length. Note that any triangle-interior points lying entirely inside the sphere should be removed, ensuring that the displaced points generated from v are given higher priority.



Further Improvements. Although treating all edges uniformly and applying the 1vN strategy ensures generality, it may introduce unnecessary computational overhead, especially in planar regions. Therefore, one may optionally pre-detect sharp feature lines by applying a dihedral angle threshold, and restrict the use of the 1vN strategy to those regions only.

Furthermore, similar to the vertex-based strategy that uses a small enclosing sphere, we use a thin cylinder, with a radius of $\rho \cdot l$, to enclose each mesh edge for generating displaced points. As shown in the inset figure, the cylinder intersects the base surface along two straight lines. Base points are extracted from these lines, and corresponding displaced points are then generated. It is important to remove any base sample points that lie entirely inside the cylinder to ensure a clean, artifact-free offset surface.



In Figure 7, we visualize the base sample points, along with the displaced points corresponding to vertex-type and edge-type base points. As indicated by the CD, HD, and NC scores annotated in the figure, our 1vN sampling strategy effectively handles complex sharp features, producing accurate offset surfaces. Additionally, we provide an ablation study on how accuracy depends on sampling density in Section 5.3.

4.2 Misalignment Elimination

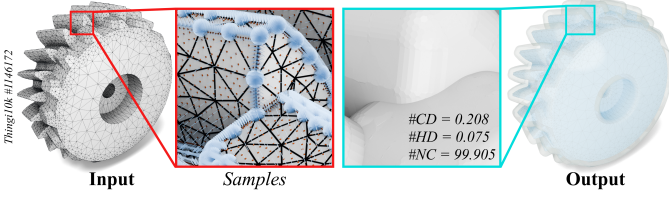
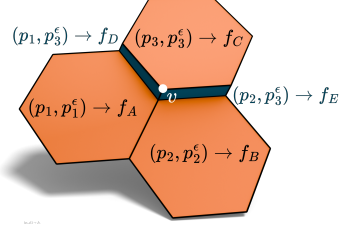


Fig. 7: Our 1vN sampling strategy effectively handles complex sharp features, resulting in accurate offset surfaces. See the CD, HD, and NC scores annotated in the figure. Note that CD is scaled by 10^4 , and both HD and NC are scaled by 10^2 .

As mentioned in the previous section, misaligned facets often arise in crust-based approaches. Consider the inset figure as an example: each facet is defined by one on-surface point and one off-surface point. The vertex v of the power diagram is incident to three facets: f_C , f_D , and f_E , where f_C is formed by p_3 and its displaced point, f_D by p_1 and the displaced point of p_3 , and f_E by p_2 and the displaced point of p_3 . This example illustrates that misaligned facets result from competition between one base point and the displaced point of another base point.



Generally, each facet incident to the vertex v is defined by a pair of sites: one being a base point and the other a displaced point. The two sites may either be a matched pair (e.g., p_3 and its displaced point), or they may not be paired (e.g., p_1 and the displaced point of p_3). Let $\{p_i\}_{i=1}^k$ denote the set of all base points contributing to a vertex v . Ideally, we want v to lie at a distance $d_i := \mathcal{R}(p_i)$ from the tangent plane at each p_i . Let $\mathbf{n}_i^{\text{off}} := \mathbf{n}_{\mathcal{R}}^{\text{off}}(p_i)$ denote the corresponding offset direction.

Formally, we aim to minimize the deviation of the expression:

$$(v - p_i) \cdot \mathbf{n}_i^{\text{off}} - d_i, \quad (13)$$

which should be as close to zero as possible. This leads naturally to the following least-squares optimization problem:

$$\min_v \sum_{i=1}^k \left((v - p_i) \cdot \mathbf{n}_i^{\text{off}} - d_i \right)^2. \quad (14)$$

It can be imagined that when the directions $\{\mathbf{n}_i^{\text{off}}\}$ are nearly identical, the solution may not be unique. This ambiguity can be resolved by encouraging v to remain close to its original position v_0 , which leads to a regularized formulation:

$$\min_v \sum_{i=1}^k \left((v - p_i) \cdot \mathbf{n}_i^{\text{off}} - d_i \right)^2 + \lambda \|v - v_0\|^2, \quad (15)$$

where λ is a small positive constant, typically set to 10^{-4} .

As long as $\lambda \neq 0$, the solution v^* exists and is unique, and is given by:

$$v^* = \mathbf{H}^{-1}(\lambda v_0 + \mathbf{b}), \quad (16)$$

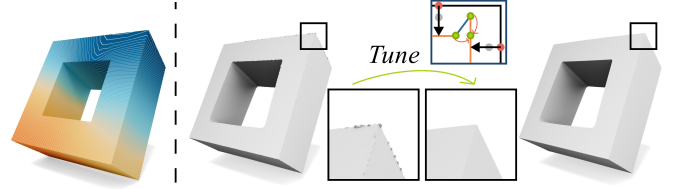


Fig. 8: Inward offset of a cube with a square hole, visualized using color-coded varying offset distances. Our misalignment elimination strategy effectively optimizes vertex positions while preserving the sharp features of the offset surface.

where

$$\mathbf{H} = \sum_{i=1}^k \mathbf{n}_i^{\text{off}} (\mathbf{n}_i^{\text{off}})^T + \lambda \mathbf{I}, \quad (17)$$

and

$$\mathbf{b} = \sum_{i=1}^k (p_i \cdot \mathbf{n}_i^{\text{off}} + d_i) \mathbf{n}_i^{\text{off}}. \quad (18)$$

Similar to the Quadric Error Metrics (QEM) method [38], the derivation can also be expressed using homogeneous coordinates.

As illustrated in Figure 8, the vertices are initially misaligned before refinement (see the close-up windows). Our misalignment elimination strategy effectively optimizes vertex positions, preserving the sharp features of the offset surface. However, it should be noted that triangle quality may degrade as a side effect of this optimization. Further discussion is provided in the Appendix D.

5 EVALUATION

Platform. We implemented our method in C++ using CGAL [39], employing the *Exact Predicates Exact Constructions Kernel* for robust power diagram computations, accelerated using Intel TBB [40]. For the misalignment elimination step, we use Eigen’s LDLT solver [41], parallelized with OpenMP [42]. We also leverage AABB trees, PQP [43], and libigl [44] to support distance and inside-outside queries. All experiments were conducted on a machine with an Intel i9-13900K CPU and 64 GB of RAM, running Windows 11.

Parameter Setting. For triangle mesh inputs, we use blue noise sampling to select 70K points and set the parameters as follows: $\lambda = 0.01$, $\epsilon = 10^{-6}$, $\rho = 5\%$, and a discrete spherical surface with 642 vertices. We define a relative offset distance parameter δ with respect to the bounding box diagonal length l_{diag} , such that the absolute offset distance is given by $d = \delta \cdot l_{\text{diag}}$. All input triangle meshes are preprocessed using TetWild [45], [46] with the edge length parameter set to $l = 0.5$. We denote results without misalignment elimination as “Ours”, and those with this step as “Ours+”.

Evaluation Metrics. The accuracy of constant-radius offsets is commonly evaluated by sampling the offset surface and measuring distances to the original surface. However, for variable-radius offsets, the displacement direction may not align with the projection direction, making accuracy evaluation difficult—unless the input surface and radius function are specifically constructed to allow it. Therefore,

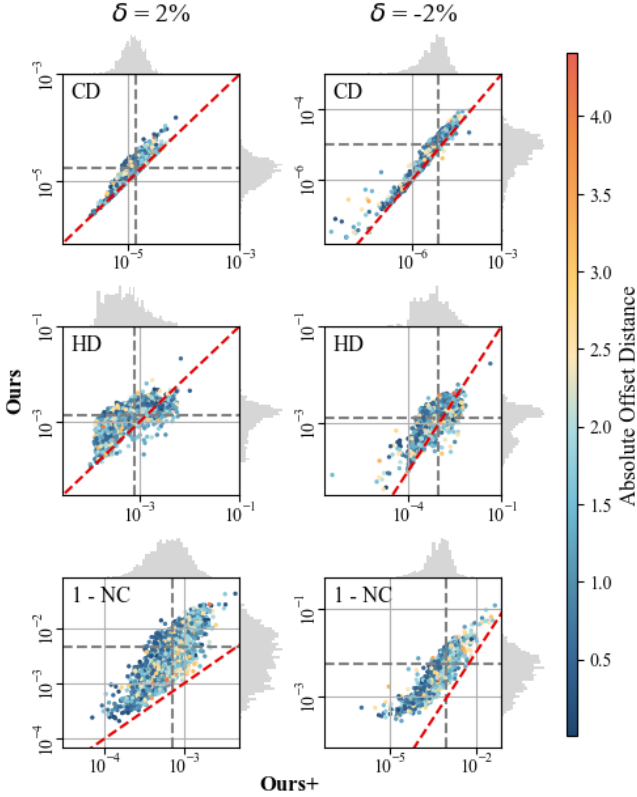


Fig. 9: Quantitative results for constant-radius offsets with $\delta = \pm 2\%$, evaluated on 2,000 models from Thingi10K, demonstrating accuracy and robustness. The gray dashed line marks the average value, and the red line represents the identity line ($y = x$). Points above the red line indicate improvement after optimization.

we restrict \mathcal{R} to be constant when evaluating the accuracy of our algorithm.

For this evaluation, we implement a one-sided error estimation metric. Specifically, we sample 100K points from the offset surface and compute their projection points onto the original surface, then calculate the projection distances $\mathbf{D}(x)$. Accuracy is measured using the normalized distance metric $|\mathbf{D}(x) - d|$, where $d = \delta \cdot l_{\text{diag}}$.

To quantitatively evaluate our results, we adopt three standard metrics: *Chamfer Distance* (CD), *Hausdorff Distance* (HD), and *Normal Consistency* (NC). CD measures the average squared nearest-neighbor distance, HD captures the maximum squared nearest-neighbor distance, and NC evaluates the alignment of surface normals, computed as the average absolute dot product between corresponding normal vectors.

5.1 Robustness and Performance

To ensure both quality and diversity of the input meshes, we conducted experiments on the preprocessed Thingi10K dataset [22]. We randomly selected 2k closed, manifold meshes that are free of self-intersections and remain consistent with their original geometry. Using default settings, we evaluated our method on relative constant offset distances $\delta = \pm 2\%$. This large-scale evaluation further supports the

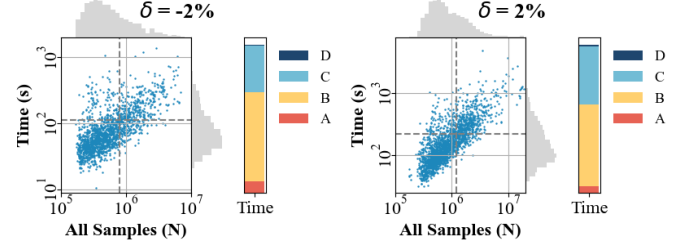


Fig. 10: Runtime performance of constant-radius offsets with $\delta = \pm 2\%$ tested on 2k models from Thingi10K. The overall runtime is shown on the *left*, while the time breakdown proportions are illustrated on the *right*.

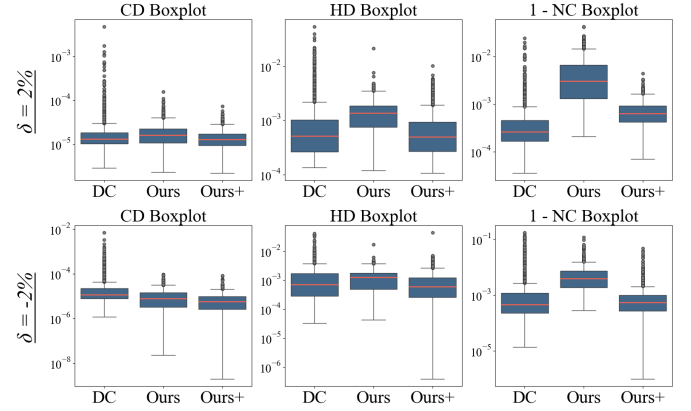


Fig. 11: Boxplots comparing dual contouring and our method on 2K models from Thingi10K with constant-radius offsets $\delta = \pm 2\%$.

effectiveness of our default settings across typical mesh inputs.

Quantitative Results and Optimization Impact. The quantitative results are presented in Figure 9. With relative distances $\delta = \pm 2\%$, various actual offset distances d were tested, consistently demonstrating reasonable accuracy and stability. Before optimization, the method performed well on the distance metrics, CD and HD, indicating that the generated shape closely aligns with the definition of an offset. After optimization, the averages and the distribution of CD and HD show minimal changes, while the NC metric exhibits significant improvement, improving by approximately an order of magnitude. In general, the initial offset surface achieves reasonable accuracy, but its quality improves significantly after optimization.

Performance. Figure 10 shows the runtime performance. The runtime increases as more points are included in the power diagram computation. The average computation time is approximately 100 seconds, with an average of 10^6 samples. Specifically, our method comprises four major steps: sampling (A), power diagram computation (B), face extraction and adjacency information retrieval (C), and optimization (D). Figure 10 (right) illustrates the time breakdown for each step.

Specifically, steps A and D consume only a small fraction of the total runtime. Apart from step B, step C is particularly time-consuming. This step is essential for preparing the data

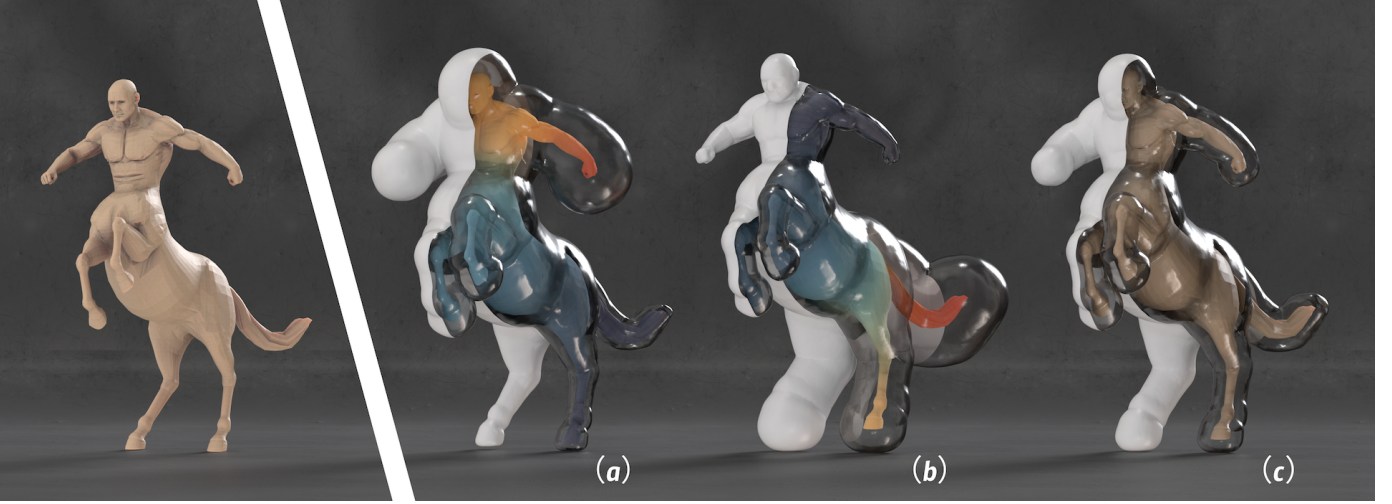


Fig. 12: By assigning varying offset distances (visualized using different colors) to the vertices of the input Centaur model, our method generates a set of outward variable-radius offset surfaces: (a) the front part is enlarged significantly more than the rear, (b) the rear part is enlarged significantly more than the front, and (c) a constant-radius offset is applied uniformly across the model.

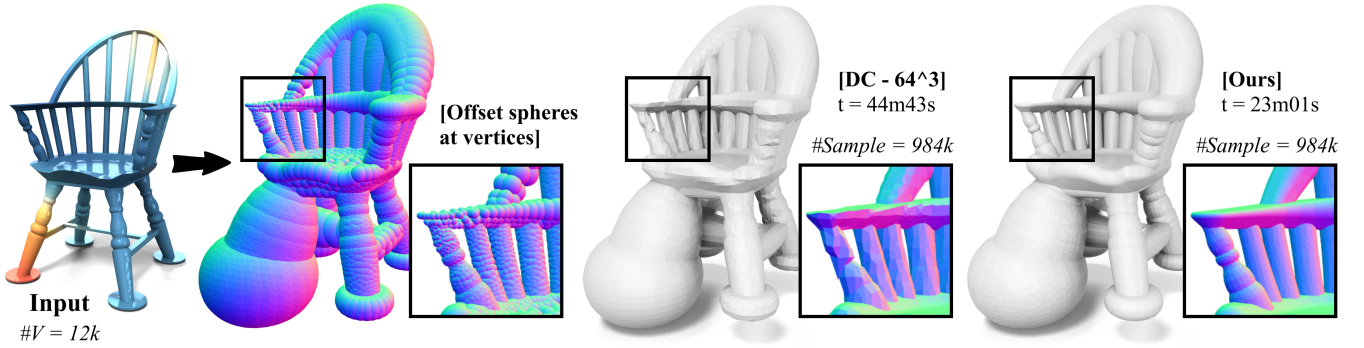


Fig. 13: Chair with offset distances defined at the vertices. (a) When only offset balls centered at vertices are used, the reconstruction exhibits spherical artifacts. Using the same sample points, (b) dual contouring [6] with a resolution of 64^3 takes 44 minutes and yields suboptimal results with prominent artifacts, mainly due to the costly direct distance queries from grid points to sample points required to construct the variable-offset distance field (see Eq. 1), while (c) our method completes in 23 minutes and achieves superior quality. Note that we visualize the normal vectors in a color-coded fashion, for better exhibiting the surface quality.

for optimization, specifically extracting the polygonal facets and the adjacency information for each vertex within the facets.

Comparisons with Dual Contouring. For comparison, we use dual contouring (DC) [6] at a resolution of 300^3 as the baseline and evaluate on 2K models with offset distances $\delta = \pm 2\%$. Specifically, we first compute the signed distance to the input mesh at each grid point, forming a scalar field over the grid. We then extract the offset surface as the level set at distance d using dual contouring.

Figure 11 presents boxplots comparing the performance metrics of DC and our method (with and without misalignment elimination). For CD and HD, our method is comparable to DC in median and interquartile range. Notably, our method achieves smaller minimum and maximum values, and the range of outliers is also smaller than DC’s, indicating better accuracy and more stable performance. For NC, although our method improves significantly after eliminating misalignments, it performs better than DC on inward

offsets, while the outward offsets do not outperform DC. However, since these differences are within an acceptable range and our method exhibits fewer outliers, the results remain favorable.

5.2 Effectiveness of Variable-Radius Offsets

Our method supports variable-radius offsets on triangle meshes, with offset distances specified per-vertex or over the surface in a flexible manner. Figure 2 shows inward and outward offsets where distances are defined by a quadratic function at the vertices. These results demonstrate effectiveness on both CAD models with sharp features and organic shapes with complex geometry. By assigning distances at selected vertices and interpolating them using the biharmonic equation ($\Delta^2 \mathcal{R} = 0$), our method enables flexible, intuitive modeling of diverse and expressive surface structures. As illustrated in Figure 12, this makes our approach well-suited for customized freeform design. We also showcase offset

TABLE 1: Ablation studies on the smooth kitten model to examine the effects of the number of blue noise samples, and on the sharp block model to test the size of the protected sharp regions and the level of sphere discretization. The gray-filled cells show scores of optimized results. Among these, the best scores are emphasized in **bold**, while the second-best scores are highlighted in **bold**. For the ablation study of block model, **blue** data indicate significant changes in the scores for each group of settings.

| Ours / Ours+ | | Kitten (Smooth) | | | | | | | | Block (Sharp Features) | | | | | | | | | | | |
|--------------|------------------------|-----------------|-------------|----------------|--------------|----------------|---------------|----------------|---------------|------------------------|---------------|----------------|---------------|----------------|---------------|---------------------------------|---------------|----------------|---------------|----------------|---------------|
| Settings | | B ₁ | | B ₂ | | B ₃ | | B ₄ | | R ₁ | | R ₂ | | R ₃ | | R ₄ , S ₂ | | S ₃ | | S ₁ | |
| | | #blue = 35K | #blue = 70K | #blue = 140K | #blue = 550K | | | | | NaN | | $\rho = 70\%$ | $\rho = 30\%$ | | | $\rho = 5\%, \#SV = 642$ | | #SV = 2562 | #SV = 162 | | |
| -4% | CD ($\times 10^4$) ↓ | 0.463 | 0.442 | 0.297 | 0.277 | 0.188 | 0.161 | 0.046 | 0.044 | 4.276 | 3.986 | 4.225 | 3.922 | 4.190 | 3.866 | 4.050 | 3.901 | 2.475 | 2.170 | 11.365 | 11.616 |
| | HD ($\times 10^2$) ↓ | 0.452 | 0.394 | 0.332 | 0.349 | 0.277 | 0.256 | 0.078 | 0.054 | 2.751 | 1.150 | 2.752 | 1.061 | 2.539 | 1.081 | 3.449 | 1.091 | 3.358 | 1.040 | 3.134 | 3.053 |
| | NC ($\times 10^2$) ↑ | 98.237 | 99.654 | 98.538 | 99.699 | 98.658 | 99.725 | 99.719 | 99.930 | 99.258 | 99.902 | 99.416 | 99.907 | 99.446 | 99.908 | 99.384 | 99.914 | 99.471 | 99.921 | 99.187 | 99.841 |
| | Time (s) | 44.535 | | 68.653 | | 107.935 | | 254.460 | | 20.805 | | 25.697 | | 27.910 | | 47.452 | | 89.990 | | 40.651 | |
| 4% | CD ($\times 10^4$) ↓ | 0.600 | 0.569 | 0.324 | 0.303 | 0.186 | 0.162 | 0.029 | 0.028 | 7.604 | 6.987 | 7.680 | 7.034 | 7.563 | 7.139 | 7.235 | 7.148 | 2.640 | 2.436 | 27.176 | 28.004 |
| | HD ($\times 10^2$) ↓ | 0.320 | 0.310 | 0.224 | 0.287 | 0.145 | 0.080 | 0.035 | 0.033 | 1.665 | 0.799 | 2.719 | 0.872 | 1.660 | 0.783 | 1.932 | 0.908 | 1.800 | 0.773 | 3.276 | 2.970 |
| | NC ($\times 10^2$) ↑ | 98.480 | 99.705 | 98.661 | 99.737 | 98.823 | 99.763 | 99.828 | 99.962 | 99.359 | 99.869 | 99.517 | 99.877 | 99.582 | 99.877 | 99.530 | 99.877 | 99.693 | 99.902 | 98.999 | 99.657 |
| | Time (s) | 34.090 | | 54.574 | | 105.528 | | 275.462 | | 46.316 | | 62.449 | | 63.389 | | 141.155 | | 209.596 | | 86.397 | |
| -0.5% | CD ($\times 10^4$) ↓ | 0.261 | 0.234 | 0.140 | 0.125 | 0.076 | 0.068 | 0.004 | 0.005 | 4.312 | 4.098 | 2.237 | 2.054 | 1.149 | 0.709 | 1.409 | 0.664 | 1.349 | 0.644 | 1.419 | 0.740 |
| | HD ($\times 10^2$) ↓ | 0.129 | 0.085 | 0.100 | 0.074 | 0.053 | 0.049 | 0.006 | 0.005 | 11.375 | 9.506 | 10.558 | 7.544 | 5.763 | 1.103 | 7.602 | 2.442 | 6.593 | 3.247 | 6.545 | 4.442 |
| | NC ($\times 10^2$) ↑ | 98.541 | 99.774 | 98.915 | 99.796 | 99.045 | 99.802 | 99.887 | 99.976 | 98.925 | 99.720 | 99.236 | 99.847 | 99.423 | 99.954 | 99.397 | 99.961 | 99.382 | 99.961 | 99.397 | 99.951 |
| | Time (s) | 95.022 | | 121.724 | | 172.397 | | 360.744 | | 34.322 | | 45.352 | | 41.786 | | 69.991 | | 96.635 | | 55.133 | |
| 0.5% | CD ($\times 10^4$) ↓ | 0.290 | 0.266 | 0.152 | 0.137 | 0.081 | 0.072 | 0.004 | 0.004 | 13.033 | 15.306 | 5.957 | 6.649 | 0.949 | 1.097 | 0.665 | 0.723 | 0.587 | 0.635 | 1.048 | 1.085 |
| | HD ($\times 10^2$) ↓ | 0.137 | 0.115 | 0.077 | 0.048 | 0.048 | 0.031 | 0.006 | 0.004 | 15.776 | 16.139 | 16.357 | 11.761 | 4.461 | 1.243 | 7.655 | 0.411 | 8.837 | 1.097 | 7.910 | 0.570 |
| | NC ($\times 10^2$) ↑ | 98.593 | 99.759 | 98.910 | 99.781 | 98.998 | 99.790 | 99.864 | 99.973 | 97.530 | 98.899 | 98.452 | 99.480 | 99.497 | 99.927 | 99.698 | 99.964 | 99.687 | 99.968 | 99.672 | 99.944 |
| | Time (s) | 53.826 | | 74.450 | | 126.879 | | 312.150 | | 72.416 | | 86.086 | | 76.644 | | 151.134 | | 364.322 | | 106.454 | |

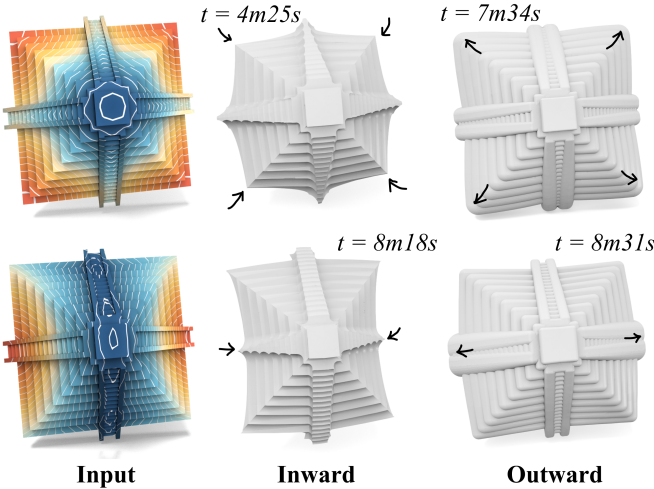


Fig. 14: The simple pyramid is deformed into different shapes by specifying larger offsets at four positions on the top and two positions on the bottom.

results generated by specifying flexible per-vertex distances. Figure 14 demonstrates how this method can deform a simple pyramid into different shapes.

As shown in Figure 13, our method offers flexible control over offset behavior, robustly handles topological changes and geometric features, and enables the generation of structured, expressive geometries for freeform modeling. It is also obvious that insufficient sampling, such as using only the mesh vertices, results in spherical artifacts. With the same dense samples on the mesh, dual contouring with a resolution of 64^3 takes 44 minutes and yields suboptimal results, since it directly queries distances from grid points to sample points according to Eq. 1 to construct the distance field for the variable-offset surface. In contrast, our method

completes in 23 minutes and achieves superior quality.

For continuous input based on a parametric curve, Figure 16 presents an example constructing a *Dupin cyclide*, a classic geometric surface well-suited for variable-radius offset modeling. This example effectively demonstrates that increasing the sampling density along the curve and using a higher-resolution Slerp-based 1vN samples leads to more accurate surface reconstruction. Notably, even with a finite number of samples, our method produces topologically correct surfaces without artifacts such as fractures caused by offset spheres.

5.3 Ablation Study

In our method, sampling plays a crucial role in determining the quality of the results. Specifically, our approach relies on four key components: blue noise sampling, clearance parameter ρ , the level of 1vN sampling, and the dihedral angle threshold for detecting sharp feature lines.

Number of Blue-Noise Sampling. Blue-noise sampling uniformly captures the overall shape of the input model. To evaluate its effectiveness, we tested it on a smooth and detailed shape, *Kitten* (Figure 17). In general, denser sample points yield better results, regardless of whether the offset distance is small or large (Table 1, left). However, this improvement comes at the cost of increased computation time.

Clearance Parameter ρ . As shown in Table 1, this approach is particularly effective for small offset distances, with accuracy improving significantly as ρ decreases. Figure 15 (left) illustrates the results for $\delta = -0.5\%$.

Without setting safe bands, excessive sampling from the discrete sphere leads to noticeable protrusions. Even with misalignment elimination, these artifacts cannot be fully corrected. However, reducing ρ results in smoother regions, even without the elimination step. In addition, concave regions can retain sharpness through optimization, and an

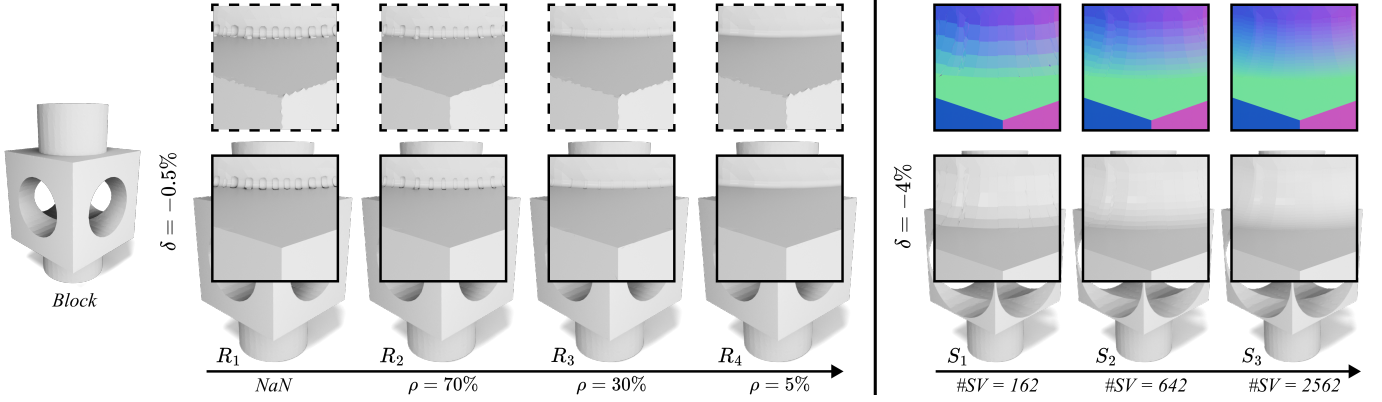


Fig. 15: For the ablation study on the block model with sharp features, we use a high-quality mesh with $\#F = 40K$ and adopt centroids as blue-noise samples. The solid box displays the optimized results, while the dashed box shows the results before optimization. For small offset distances $\delta = -0.5\%$, a smaller ρ can better handle the rounding behavior of sharp regions, reducing the side effects introduced by excessive samples from the discrete sphere (left). For large offset distances $\delta = -4\%$, a more finely discretized sphere with more vertices can provide smoother and more precise results (right).

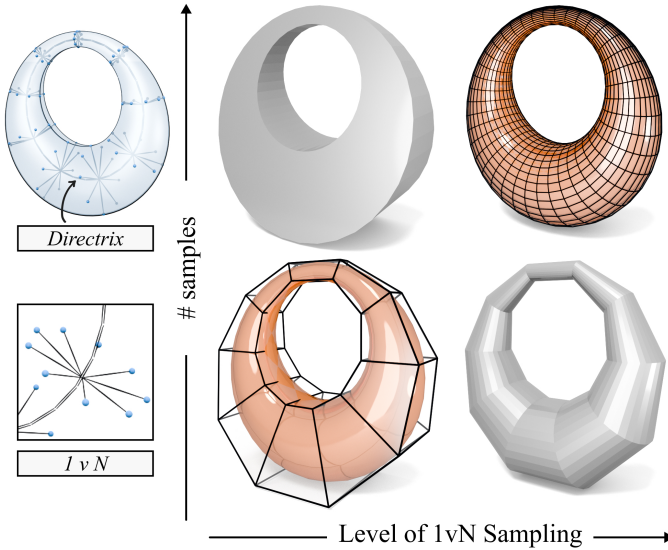


Fig. 16: Construction of a Dupin cyclide surface using 1vN sampling from its directrix. Increasing the sampling density results in finer discretization and improved geometric accuracy.

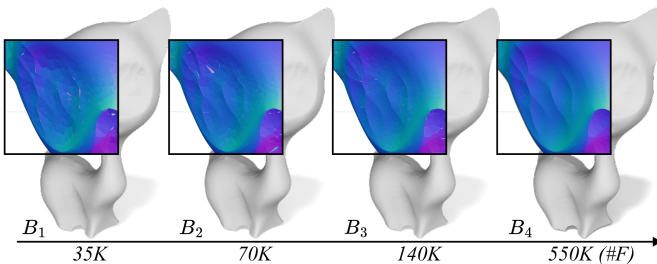


Fig. 17: Different numbers of blue noise samples for the kitten model at a distance of $\delta = -4\%$. With more samples, the results are smoother and more reliable.

appropriate choice of ρ can help preserve desirable features even before optimization is applied. We empirically found that smaller offset distances benefit from a smaller ρ , which

TABLE 2: Ablation study on the Fandisk model evaluating the effects of our dihedral angle-based Convexity-Based Filtering.

| Dihedral ($rad/^\circ$) | NaN | 0.2 / 11° | 0.5 / 29° | 1 / 57° | 1.5 / 86° |
|---------------------------|--------|------------------|------------------|----------------|------------------|
| All Samples | 831K | 425K | 378K | 371K | 340K |
| CD ($\times 10^4$) ↓ | 0.099 | 0.105 | 0.134 | 0.175 | 2.213 |
| HD ($\times 10^2$) ↓ | 0.040 | 0.042 | 0.106 | 0.491 | 4.446 |
| NC ($\times 10^2$) ↑ | 99.959 | 99.944 | 99.936 | 99.924 | 99.341 |
| Time (s) | 89.938 | 54.923 | 50.057 | 51.079 | 43.352 |

better preserves sharp geometric features, while larger offsets can tolerate a relatively larger ρ without introducing noticeable artifacts.

Level of 1vN Sampling. The discrete Gaussian spherical surface is used to generate rounded shapes around edges and vertices. For constant-radius offsets, we adopt a hybrid strategy that combines spherical sampling with Slerp-based 1vN interpolation. To evaluate the effect of the discretization level, we associate each Slerp interpolation with the corresponding resolution of the sphere.

As shown in Table 1, increasing the discretization level consistently improves accuracy across all offset distances, with more pronounced effects observed at larger distances. Figure 15 (right) illustrates the case for $\delta = -4\%$. As more vertices are incorporated into the spherical surface, the rounded regions naturally become smoother.

Dihedral Angle Threshold for Identifying Feature Lines. To reduce computational overhead, we optionally pre-detect sharp features using a dihedral angle threshold, and apply the 1vN strategy only to those regions.

To evaluate its effectiveness, we conduct an ablation study using the *Fandisk* model, which features intricate sharp structures, as shown in Figure 18. All evaluation metrics and experimental settings are summarized in Table 2.

Results indicate that disabling the filtering improves output quality, but at the cost of significantly increased computation time. As the dihedral angle threshold increases, fewer samples are retained around edges and vertices. This reduction lowers computational cost but leads to a decline in quality, particularly as the threshold approaches a right angle. To balance quality and efficiency, we adopt a dihedral

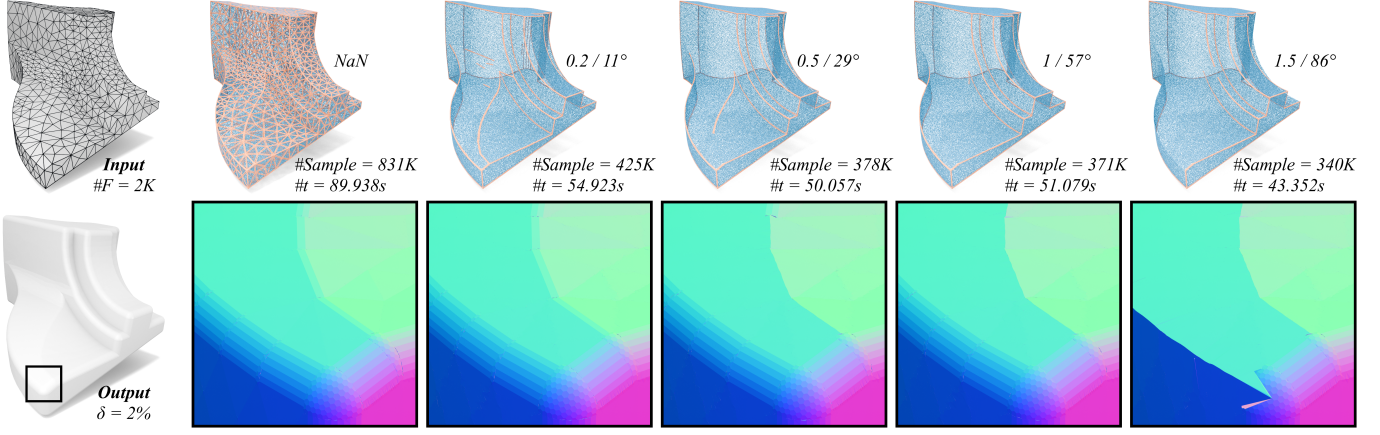


Fig. 18: Ablation study on the Fandisk model with dihedral angle threshold for filtering.

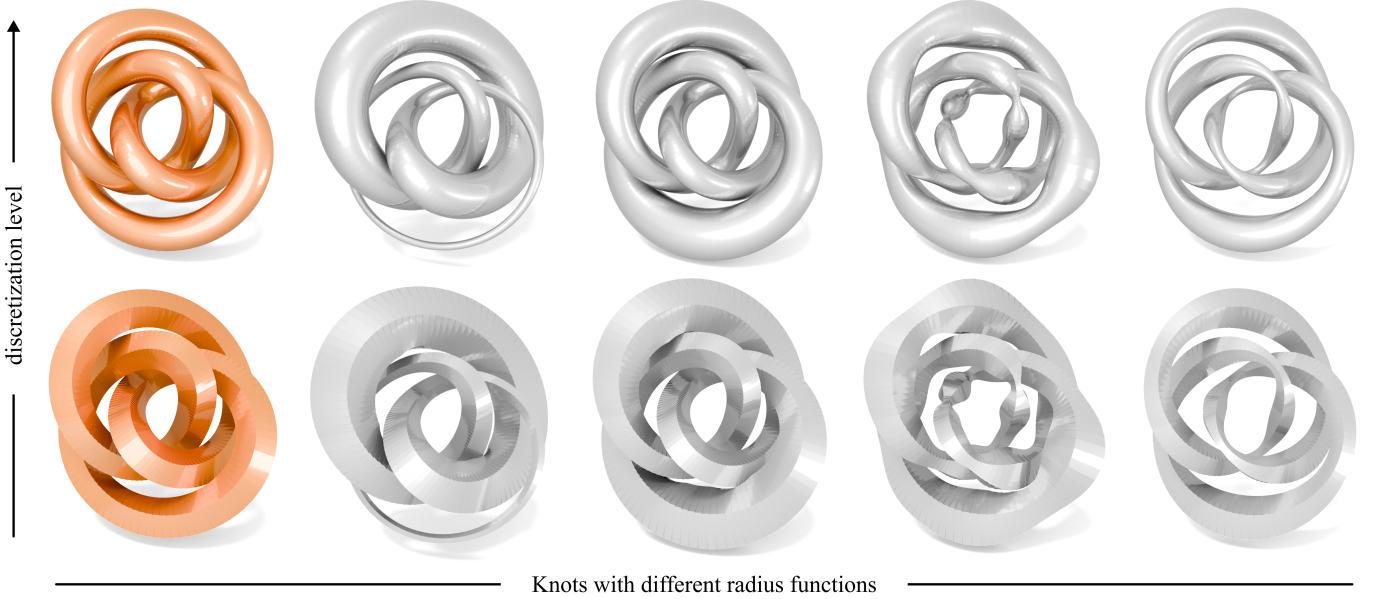


Fig. 19: Construction of diverse knots from a parameterized central curve, defined as $x = (2 + \cos(2u)) \cos(3u)$, $y = (2 + \cos(2u)) \sin(3u)$, and $z = \sin(4u)$, with 300 sample points. From left to right, the radius functions vary as follows: (a) $\mathcal{R}(u) = 0.45$ (constant radius), (b) $\mathcal{R}(u) = 0.4 + 0.3 \cos(u)$, (c) $\mathcal{R}(u) = 0.4 + 0.3e^{-5 \sin^2(u)}$, (d) $\mathcal{R}(u) = 0.4 + 0.15 \cos(2u) + 0.1 \sin(13u + \cos(u)) + 0.05 \sin(20u)$, (e) $\mathcal{R}(u) = 0.3 + 0.1 \cos(2u) + 0.1 \cos(8u)$. *Top*: limiting displacement directions to 150 possibilities. *Bottom*: limiting displacement directions to only 5 possibilities.

angle threshold of 0.2 radians in all our experiments.

6 APPLICATIONS

In this section, we demonstrate the applicability of *OffsetCrust* across a variety of modeling tasks, including channel modeling, MAT-based surface reconstruction, and feature-preserving morphological operators.

6.1 Offset-Based Channel Surface Modeling

Channel surfaces are formed as the envelopes of spheres whose centers lie along a curve known as the *directrix* [47]. Using our *OffsetCrust* method, we begin with a user-specified curve and an associated smooth radius function. The method provides flexibility in defining non-uniform radius profiles, enabling the modeling of complex shapes.

In Figure 19, we generate diverse knot models by varying the radius function while keeping the directrix fixed. Furthermore, we can intentionally reduce the number of displacement directions: the top row of Figure 19 limits displacement directions to 150, while the bottom row further reduces them to just 5, resulting in a faceted offset surface.

6.2 Surface Reconstruction from Medial Axis Transform

As a shape descriptor [48]–[50], the medial axis transform (MAT) offers a compact representation of a shape’s topology and structure. In the discrete setting, the MAT surface consists of vertices, edges, and faces, with an associated radius defined at each vertex. Despite significant progress in computing MATs, recovering the original boundary surface from a given MAT remains a challenging problem.

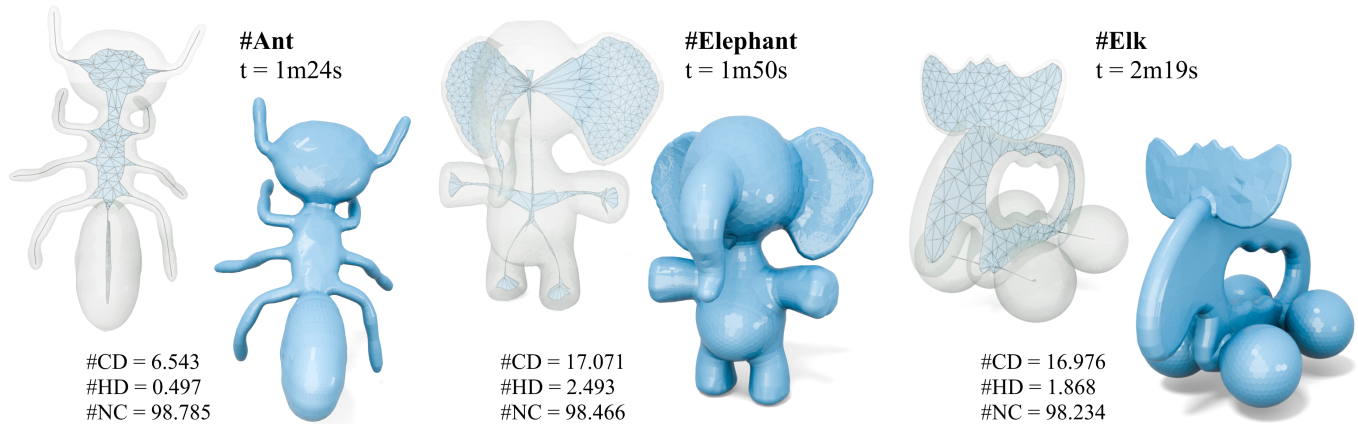


Fig. 20: Surface reconstruction from medial axis transforms (MATs) generated using variable-radius offsets computed by our method. The MATs are produced by Q-MAT [48], and the reconstructed surfaces faithfully preserve the geometry of the original shapes. In these examples, we use 5K blue noise samples for on-surface sampling.

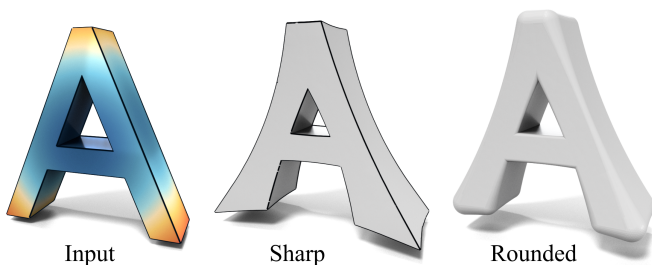


Fig. 21: Given the letter “A” (left), *OffsetCrust* can produce either a feature-preserved offset (middle) or a rounded-feature offset (right) by controlling the displacement directions when generating edge-around and vertex-around displaced points.

In fact, this task can be formulated as a variable-radius offsetting problem, where the base surface is the MAT itself, and the radius function naturally satisfies $\|\nabla \mathcal{R}\| < 1$. Figure 20 presents surface reconstruction results, where the input MATs are generated using Q-MAT [48]. We evaluate the reconstruction quality by computing the two-sided distance between the original boundary surface and the reconstructed surface. Based on the CD, HD, and NC scores shown in the figure, it is evident that our *OffsetCrust* method accurately recovers the geometry of the original boundary surface.

6.3 Feature-preserved Opening and Closing

Recall that when generating edge-around and vertex-around base samples, we employ a Slerp-like technique to produce displaced points. In fact, we can further restrict the set of allowable displacement directions. In extreme cases, intermediate directions can be skipped entirely, resulting in a *feature-preserved* offset shape. For example, in Figure 21, we use the letter “A” as input and generate both a feature-preserved offset and a rounded-feature offset.

We extend this behavior to morphological operations such as opening and closing. It is well known that closing consists of dilation followed by erosion, while opening is

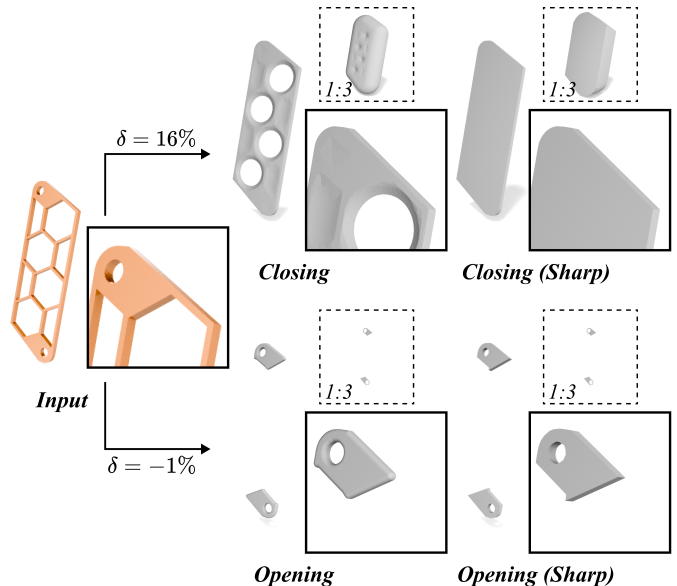


Fig. 22: Both opening and closing are morphological operations: closing combines dilation followed by erosion, while opening is defined vice versa. By controlling the displacement directions, our *OffsetCrust* can produce both standard smooth outcomes and sharp-featured variants.

defined in the reverse order. By similarly controlling the displacement directions, our *OffsetCrust* can produce both standard smooth outcomes and sharp-featured variants. See Figure 22. Note that δ denotes the relative offset distance.

7 DISCUSSION AND LIMITATIONS

In this paper, we presented *OffsetCrust*, a crust-based method for explicitly computing variable-radius offset surfaces. Given the radius function \mathcal{R} , our formulation leverages power diagrams to robustly determine the offset geometry by carefully sampling base points and generating their corresponding off-surface points, displaced along \mathcal{R} -dependent directions. This approach generalizes smoothly

from the constant-radius case—where displacement directions align with surface normals—to more complex, variable-radius scenarios.

To address the misalignment issues commonly encountered in crust-based methods, we introduced a lightweight fine-tuning procedure that significantly improves geometric fidelity. Through extensive experiments, we validated the effectiveness and efficiency of our method and demonstrated its applicability in a variety of modeling tasks, including MAT-based surface reconstruction.

Despite these strengths, our method has certain limitations. First, while our misalignment elimination strategy preserves geometric features effectively, it may sometimes degrade the quality of the resulting triangulation. Second, when the input mesh contains long and thin triangles, it becomes challenging to robustly extract representative base sample points, particularly around mesh edges and vertices. Third, due to the extraction from power diagram facets, the resulting mesh quality is poor in practice, although the geometry remains accurate, as shown in Appendix A. Nevertheless, the output meshes can be further improved by applying post-processing techniques such as remeshing approaches like TetWild [46].

APPENDIX A STATISTICS OF OUTPUT MESH QUALITY

We assessed the quality of 2k output meshes in terms of manifoldness, self-intersections, and boundaries using evaluation functions from libigl. To utilize these existing functions, we triangulated the output polygonal facets. For each output, we computed the **proportions** of non-manifold edges (EN) and boundary edges (EB), non-manifold vertices (VN), and non-coplanar intersecting faces (FI) relative to the total number of edges, vertices, and faces. Table 3 shows the statistics.

Recall that a power diagram may include thin facets as its complexity increases. A few non-manifold edges and vertices, boundary edges, and self-intersections may occur due to these thin facets, but these defects do not noticeably affect accuracy (see Sec. 5.1).

TABLE 3: Statistics for $\delta = 2\%$ and $\delta = -2\%$ with raw and optimized results (ours/ours+).

| δ | Metric | EN | EB | VN | FI |
|----------|--------|---------------|-----------------|---------------|----------------|
| 2% | min | 0%/0% | 0%/0% | 0%/0% | 0.001%/2.128% |
| | mean | 0%/0.004% | 0%/0% | 0.023%/0.028% | 0.056%/9.180% |
| | max | 0.001%/0.528% | 0%/0% | 0.302%/0.540% | 6.062%/23.138% |
| -2% | min | 0%/0% | 0%/0% | 0%/0% | 0%/0.249% |
| | mean | 0%/0.002% | 0%/0% | 0.022%/0.023% | 0.076%/11.759% |
| | max | 0.002%/0.376% | 0.0003%/0.0003% | 0.367%/0.398% | 5.128%/66.176% |

APPENDIX B ANALYSIS OF MISALIGNED FACETS

Based on Section 3, we can filter the offset facets. However, due to the discontinuities in real sampling, some additional facets are also included to preserve watertightness:

$$d_{pow}(x, p_i) = d_{pow}(x, p_j^\epsilon), \quad i \neq j. \quad (19)$$

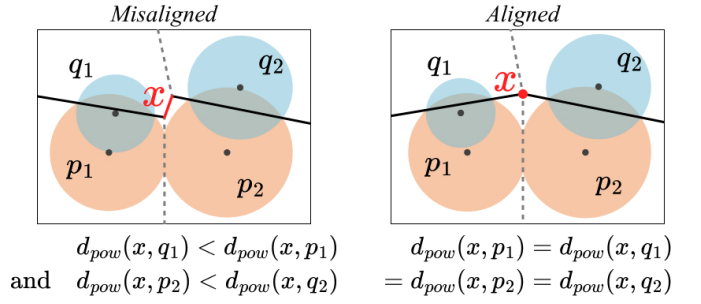


Fig. 23: Power diagram of four random sites.

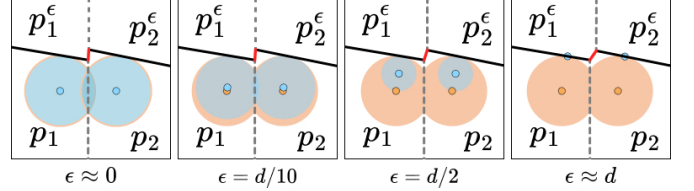


Fig. 24: Configurations of sites in *OffsetCrust*. With a larger ϵ , the misaligned facets become more oblique relative to the sites, which can easily lead to inconsistent regions between p_i and p_i^ϵ .

Meanwhile, we do not select the facets that satisfy:

$$d_{pow}(x, p_i) = d_{pow}(x, p_j), \quad i \neq j, \quad (20)$$

$$\text{or } d_{pow}(x, p_i^\epsilon) = d_{pow}(x, p_j^\epsilon), \quad i \neq j. \quad (21)$$

To completely eliminate the misaligned facets, we require that for all $x \in \{x \mid d_{pow}(x, p_i) = d_{pow}(x, p_j^\epsilon)\}$, the following must hold:

$$d_{pow}(x, p_j) \leq d_{pow}(x, p_i) = d_{pow}(x, p_j^\epsilon), \quad i \neq j, \quad (22)$$

$$\text{or } d_{pow}(x, p_i^\epsilon) \leq d_{pow}(x, p_j^\epsilon) = d_{pow}(x, p_i), \quad i \neq j. \quad (23)$$

Conversely, misaligned facets **exist** when:

$$d_{pow}(x, p_j) > d_{pow}(x, p_i) = d_{pow}(x, p_j^\epsilon), \quad i \neq j, \quad (24)$$

$$\text{and } d_{pow}(x, p_i^\epsilon) > d_{pow}(x, p_j^\epsilon) = d_{pow}(x, p_i), \quad i \neq j. \quad (25)$$

For any four random sites, to eliminate both sides of misaligned facets, the following condition must be satisfied:

$$d_{pow}(x, p_i) = d_{pow}(x, p_i^\epsilon) = d_{pow}(x, p_j) = d_{pow}(x, p_j^\epsilon). \quad (26)$$

Figure 23 demonstrates the relationship between the regions for four random sites. Misaligned facets are almost inevitable in any sampling configuration when implementing *OffsetCrust*.

Figure 24 illustrates the configuration of sites used in *OffsetCrust*. While $0 < \epsilon < \mathcal{R}(p)$ is theoretically effective, as analyzed in Section 3, selecting a small $\epsilon > 0$ improves stability when addressing misaligned facets. This is because the ϵ -balls have radii comparable to the offset balls, making their interactions with other sites more similar to prevent uncontrollable misalignments (Figure 25). As a result, local adjacency is better preserved, which benefits vertex optimization in Section 4.2.

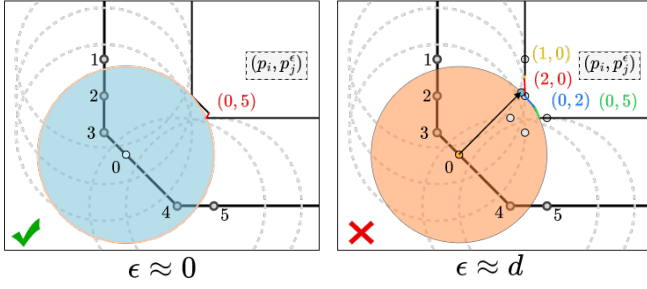


Fig. 25: With smaller ϵ , the misalignments are more localized and thus easier to optimize. In contrast, larger ϵ leads to more complex misalignment adjacencies, making optimization more difficult.

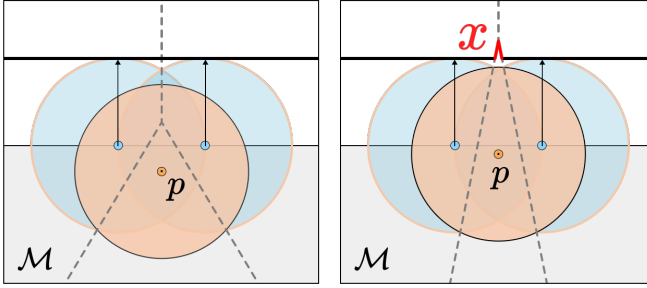


Fig. 26: 2D illustration of Figure 27. When the point p is close to the edge and has significantly different directions, misalignments arise between p and the on-edge Slerp ϵ -samples.

APPENDIX C CLEARANCE AROUND MESH EDGES

As demonstrated in Figure 26, when the point p is close to an edge and exhibits significantly different directions, misalignments can occur between p and the on-edge Slerp ϵ -samples. These misalignments may result in incorrect adjacency relationships, leading to uncontrolled artifacts and negatively impacting the normal-based optimization.

To prevent this issue, as illustrated in the inset figure, we consider the critical configuration in which the offset ball centered at point p just touches the intersection point of two on-edge samples, with the inter-sample distance denoted as r . In the constant-radius case, the safe band size is determined by the relation $d \cdot (1 - \cos \alpha) \in (0, \frac{r}{2})$, making $\frac{r}{2}$ a conservative and reliable choice. For the variable-radius case, as the samples are densely distributed and the offset distances vary smoothly, $\frac{r}{2}$ is also generally a safe and effective choice.

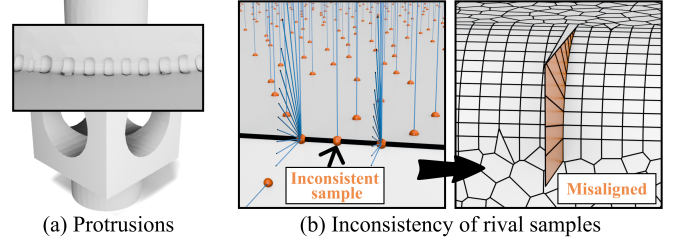
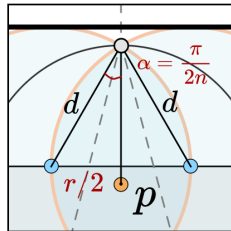


Fig. 27: Two types of undesirable behaviors affect the quality of the offset surface: (a) Protrusions caused by redundant 1vN sampling. (b) Structural misalignment caused by local inconsistency in the behavior of a 1v1 sample near the 1vN region.

APPENDIX D MISALIGNMENT ELIMINATION OPTIMIZATION

The regularized optimization terms, using the homogeneous coordinate system, can be expressed as follows:

$$E(v) = \sum_{i=1}^k ((v - p_i) \cdot \mathbf{n}_i - d)^2 + \lambda \|v - v_0\|^2 \quad (27)$$

$$= \sum_{i=1}^k ((v - p_i) \cdot \mathbf{n}_i - d)^2 + \lambda (v^T v - 2v^T v_0 + v_0^T v_0) \quad (28)$$

$$= \sum_{i=1}^k \left(\begin{bmatrix} v \\ 1 \end{bmatrix}^T \begin{bmatrix} \mathbf{n}_i \\ -p_i \cdot \mathbf{n}_i - d_i \end{bmatrix} \right)^2 + \lambda \left(\begin{bmatrix} v \\ 1 \end{bmatrix}^T \begin{bmatrix} I & 0 \\ 0 & 0 \end{bmatrix} \begin{bmatrix} v \\ 1 \end{bmatrix} + \begin{bmatrix} v \\ 1 \end{bmatrix}^T \begin{bmatrix} 2v_0 \\ v_0^T v_0 \end{bmatrix} \right) \quad (29)$$

$$= \begin{bmatrix} v \\ 1 \end{bmatrix}^T \left(\sum_{i=1}^k \begin{bmatrix} \mathbf{n}_i \\ -p_i \cdot \mathbf{n}_i - d_i \end{bmatrix} \begin{bmatrix} \mathbf{n}_i \\ -p_i \cdot \mathbf{n}_i - d_i \end{bmatrix}^T + \begin{bmatrix} \lambda I & 0 \\ 0 & 0 \end{bmatrix} \right) \begin{bmatrix} v \\ 1 \end{bmatrix} + \begin{bmatrix} v \\ 1 \end{bmatrix}^T \begin{bmatrix} -2\lambda v_0 \\ \lambda v_0^T v_0 \end{bmatrix} \quad (30)$$

$$\Rightarrow E(\tilde{v}) = \tilde{v}^T \tilde{H} \tilde{v} + \tilde{b}^T \tilde{v} \quad (31)$$

This optimization problem can be solved by converting it into the equation $E'(\tilde{v}) = 0$, the solution is derived as follows:

$$E'(\tilde{v}) = 0 \quad (32)$$

$$\Rightarrow 2\tilde{H}\tilde{v} = -\tilde{b} \quad (33)$$

$$\Rightarrow 2 \left(\sum_{i=1}^k \begin{bmatrix} \mathbf{n}_i \mathbf{n}_i^T & (-p_i \cdot \mathbf{n}_i - d_i) \mathbf{n}_i \\ (-p_i \cdot \mathbf{n}_i - d_i) \mathbf{n}_i^T & (-p_i \cdot \mathbf{n}_i - d_i)^2 \end{bmatrix} + \begin{bmatrix} \lambda I & 0 \\ 0 & 0 \end{bmatrix} \right) \begin{bmatrix} v \\ 1 \end{bmatrix} = \begin{bmatrix} 2\lambda v_0 \\ -\lambda v_0^T v_0 \end{bmatrix} \quad (34)$$

$$\Rightarrow [\sum_{i=1}^k \mathbf{n}_i \mathbf{n}_i^T + \lambda I \quad \sum_{i=1}^k (-p_i \cdot \mathbf{n}_i - d_i) \mathbf{n}_i] \begin{bmatrix} v \\ 1 \end{bmatrix} = \lambda v_0 \quad (35)$$

$$\Rightarrow \left(\sum_{i=1}^k \mathbf{n}_i \mathbf{n}_i^T + \lambda I \right) v = \lambda v_0 + \sum_{i=1}^k (p_i \cdot \mathbf{n}_i + d_i) \mathbf{n}_i \quad (36)$$

Denote $\mathbf{H} = \sum_{i=1}^k \mathbf{n}_i \mathbf{n}_i^T + \lambda I$, $\mathbf{b} = \sum_{i=1}^k (p_i \cdot \mathbf{n}_i + d_i) \mathbf{n}_i$, the solution is $v = \mathbf{H}^{-1} (\lambda v_0 + \mathbf{b})$. Since $\mathbf{n}_i \mathbf{n}_i^T$ is positive semi-definite and I is positive definite, \mathbf{H} remains positive definite (and thus invertible) for any $\lambda > 0$. The λ term is introduced to address the non-invertible issue by incorporating the initial vertex positions. As long as a small $\lambda > 0$ is chosen, the results remain stable, as its primary role is to ensure matrix invertibility.

REFERENCES

- [1] J. R. Rossignac and A. A. Requicha, "Offsetting operations in solid modelling," *Computer Aided Geometric Design*, vol. 3, no. 2, pp. 129–148, 1986.

- [2] A. K. Singh, A. Aggarwal, M. Vashisht, and R. Siddavatam, "Robot motion planning in a dynamic environment using offset non-uniform rational b-splines (nurbs)," in *2011 IEEE International Conference on Industrial Technology*. IEEE, 2011, pp. 312–317.
- [3] M. Held and S. De Lorenzo, "Weighted skeletal structures for computing variable-radius offsets," *Comput. Aided Des. Appl.*, vol. 18, pp. 875–889, 2021.
- [4] W. E. Lorensen and H. E. Cline, "Marching cubes: A high resolution 3d surface construction algorithm," in *Seminal graphics: pioneering efforts that shaped the field*, 1998, pp. 347–353.
- [5] E. Chernyaev, "Marching cubes 33: Construction of topologically correct isosurfaces," *Tech. Rep.*, 1995.
- [6] T. Ju, F. Losasso, S. Schaefer, and J. Warren, "Dual contouring of hermite data," in *Proceedings of the 29th annual conference on Computer graphics and interactive techniques*, 2002, pp. 339–346.
- [7] G. M. Nielson, "Dual marching cubes," in *IEEE visualization 2004*. IEEE, 2004, pp. 489–496.
- [8] Z. Chen, D. Panozzo, and J. Dumas, "Half-space power diagrams and discrete surface offsets," *IEEE Transactions on Visualization and Computer Graphics*, vol. 26, no. 10, pp. 2970–2981, 2019.
- [9] Z. Chen and H. Zhang, "Neural marching cubes," *ACM Transactions on Graphics (TOG)*, vol. 40, no. 6, pp. 1–15, 2021.
- [10] Z. Chen, A. Tagliasacchi, T. Funkhouser, and H. Zhang, "Neural dual contouring," *ACM Transactions on Graphics (TOG)*, vol. 41, no. 4, pp. 1–13, 2022.
- [11] A. Doi and A. Koide, "An efficient method of triangulating equi-valued surfaces by using tetrahedral cells," *IEICE TRANSACTIONS on Information and Systems*, vol. 74, no. 1, pp. 214–224, 1991.
- [12] G. M. Treece, R. W. Prager, and A. H. Gee, "Regularised marching tetrahedra: improved iso-surface extraction," *Computers & Graphics*, vol. 23, no. 4, pp. 583–598, 1999.
- [13] T. Shen, J. Gao, K. Yin, M.-Y. Liu, and S. Fidler, "Deep marching tetrahedra: a hybrid representation for high-resolution 3d shape synthesis," *Advances in Neural Information Processing Systems*, vol. 34, pp. 6087–6101, 2021.
- [14] L. Wang, X. Wang, P. Wang, S. Chen, S. Xin, J. Guo, W. Wang, and C. Tu, "Pco: Precision-controllable offset surfaces with sharp features," *ACM Transactions on Graphics (TOG)*, vol. 43, no. 6, pp. 1–16, 2024.
- [15] D. Zint, N. Maruani, M. Rouxel-Labb, and P. Alliez, "Feature-preserving offset mesh generation from topology-adapted octrees," in *Computer Graphics Forum*, vol. 42, no. 5. Wiley Online Library, 2023, p. e14906.
- [16] G. Elber, I.-K. Lee, and M.-S. Kim, "Comparing offset curve approximation methods," *IEEE computer graphics and applications*, vol. 17, no. 3, pp. 62–71, 1997.
- [17] T. Maekawa, "An overview of offset curves and surfaces," *Computer-Aided Design*, vol. 31, no. 3, pp. 165–173, 1999.
- [18] B. Pham, "Offset curves and surfaces: a brief survey," *Computer-Aided Design*, vol. 24, no. 4, pp. 223–229, 1992.
- [19] M.-S. Kim, E.-J. Park, and S.-B. Lim, "Approximation of variable-radius offset curves and its application to bézier brush-stroke design," *Computer-Aided Design*, vol. 25, no. 11, pp. 684–698, 1993.
- [20] J. Wallner, T. Sakkalis, T. Maekawa, H. Pottmann, and G. Yu, "Self-intersections of offset curves and surfaces," *International Journal of Shape Modeling*, vol. 7, no. 01, pp. 1–21, 2001.
- [21] S. Koch, A. Matveev, Z. Jiang, F. Williams, A. Artemov, E. Burnaev, M. Alexa, D. Zorin, and D. Panozzo, "Abc: A big cad model dataset for geometric deep learning," in *The IEEE Conference on Computer Vision and Pattern Recognition (CVPR)*, June 2019.
- [22] Q. Zhou and A. Jacobson, "Thing10k: A dataset of 10,000 3d-printing models," 2016.
- [23] W. Li and S. McMains, "A gpu-based voxelization approach to 3d minkowski sum computation," in *Proceedings of the 14th ACM symposium on solid and physical modeling*, 2010, pp. 31–40.
- [24] —, "A sweep and translate algorithm for computing voxelized 3d minkowski sums on the gpu," *Computer-Aided Design*, vol. 46, pp. 90–100, 2014.
- [25] —, "Voxelized minkowski sum computation on the gpu with robust culling," *Computer-Aided Design*, vol. 43, no. 10, pp. 1270–1283, 2011.
- [26] T. Van Hook, "Real-time shaded nc milling display," *ACM SIGGRAPH Computer Graphics*, vol. 20, no. 4, pp. 15–20, 1986.
- [27] H. Qu, N. Zhang, R. Shao, A. Kaufman, and K. Mueller, "Feature preserving distance fields," in *2004 IEEE Symposium on Volume Visualization and Graphics*. IEEE, 2004, pp. 39–46.
- [28] D. Pavić and L. Kobbelt, "High-resolution volumetric computation of offset surfaces with feature preservation," in *Computer Graphics Forum*, vol. 27, no. 2. Wiley Online Library, 2008, pp. 165–174.
- [29] M. Karavelas, "A robust and efficient implementation for the segment voronoi diagram," *International Symposium on Voronoi Diagrams in Science and Engineering*, 01 2004.
- [30] M. Held, *On the computational geometry of pocket machining*. Springer Science & Business Media, 1991, vol. 500.
- [31] M. Held, S. Huber, and P. Palfrader, "Generalized offsetting of planar structures using skeletons," *Computer-Aided Design and Applications*, vol. 13, no. 5, pp. 712–721, 2016.
- [32] L. Qun and J. Rokne, "Variable-radius offset curves and surfaces," *Mathematical and Computer Modelling*, vol. 26, no. 7, pp. 97–108, 1997.
- [33] A.-C. Woerl, E. Schoemer, and U. Schwanencke, "Variable-radius offset surface approximation on the gpu," 2020.
- [34] N. Amenta, S. Choi, and R. K. Kolluri, "The power crust," in *Proceedings of the sixth ACM symposium on Solid modeling and applications*, 2001, pp. 249–266.
- [35] A. Abdelkader, C. L. Bajaj, M. S. Ebeida, A. H. Mahmoud, S. A. Mitchell, J. D. Owens, and A. A. Rushdi, "Vorocrust: Voronoi meshing without clipping," *ACM Transactions on Graphics (TOG)*, vol. 39, no. 3, pp. 1–16, 2020.
- [36] —, "Sampling conditions for conforming voronoi meshing by the vorocrust algorithm," *LIPICs: Leibniz international proceedings in informatics*, vol. 99, 2018.
- [37] F. Aurenhammer, "Power diagrams: properties, algorithms and applications," *SIAM Journal on Computing*, vol. 16, no. 1, pp. 78–96, 1987.
- [38] M. Garland and P. S. Heckbert, "Surface simplification using quadric error metrics," in *Proceedings of the 24th annual conference on Computer graphics and interactive techniques*, 1997, pp. 209–216.
- [39] The CGAL Project, *CGAL User and Reference Manual*, 5.6.1 ed. CGAL Editorial Board, 2024. [Online]. Available: <https://doc.cgal.org/5.6.1/Manual/packages.html>
- [40] C. Pheatt, "Intel® threading building blocks," *Journal of Computing Sciences in Colleges*, vol. 23, no. 4, pp. 298–298, 2008.
- [41] G. Guennebaud, B. Jacob et al., "Eigen v3," <http://eigen.tuxfamily.org>, 2010.
- [42] L. Dagum and R. Menon, "Openmp: an industry standard api for shared-memory programming," *Computational Science & Engineering*, IEEE, vol. 5, no. 1, pp. 46–55, 1998.
- [43] E. Larsen, S. Gottschalk, M. C. Lin, and D. Manocha, "Fast proximity queries with swept sphere volumes," Technical Report TR99-018, Department of Computer Science, University of ..., Tech. Rep., 1999.
- [44] A. Jacobson, D. Panozzo et al., "libigl: A simple C++ geometry processing library," 2018, <https://libigl.github.io/>.
- [45] Y. Hu, Q. Zhou, X. Gao, A. Jacobson, D. Zorin, and D. Panozzo, "Tetrahedral meshing in the wild," *ACM Trans. Graph.*, vol. 37, no. 4, p. 60, 2018.
- [46] Y. Hu, T. Schneider, B. Wang, D. Zorin, and D. Panozzo, "Fast tetrahedral meshing in the wild," *ACM Trans. Graph.*, vol. 39, no. 4, Jul. 2020.
- [47] M. Peternell and H. Pottmann, "Computing rational parametrizations of canal surfaces," *Journal of Symbolic Computation*, vol. 23, no. 2-3, pp. 255–266, 1997.
- [48] P. Li, B. Wang, F. Sun, X. Guo, C. Zhang, and W. Wang, "Q-mat: Computing medial axis transform by quadratic error minimization," *ACM Transactions on Graphics (TOG)*, vol. 35, no. 1, pp. 1–16, 2015.
- [49] N. Wang, B. Wang, W. Wang, and X. Guo, "Computing medial axis transform with feature preservation via restricted power diagram," *ACM Transactions on Graphics (TOG)*, vol. 41, no. 6, pp. 1–18, 2022.
- [50] N. Wang, H. Huang, S. Song, B. Wang, W. Wang, and X. Guo, "Mat-topo: Topology-preserving medial axis transform with restricted power diagram," *ACM Transactions on Graphics (TOG)*, vol. 43, no. 4, 2024.